Hydrophilic Cu_9S_5 Nanocrystals: A Photothermal Agent with a 25.7% Heat Conversion Efficiency for Photothermal Ablation of Cancer Cells *in Vivo*

Qiwei Tian,[†] Feiran Jiang,[†] Rujia Zou,[†] Qian Liu,[†] Zhigang Chen,[†] Meifang Zhu,[†] Shiping Yang,[‡] Jinglong Wang,[§] Jianhua Wang,[§] and Junqing Hu[†,*]

[†]State Key Laboratory for Modification of Chemical Fibers and Polymer Materials, College of Materials Science and Engineering, Donghua University, Shanghai 201620, China, [‡]Department of Chemistry, Shanghai Normal University, Shanghai 200234, China, and [§]Department of Biochemistry and Molecular Cell Biology, Shanghai Jiao-Tong University School of Medicine, Shanghai 200025, China

ABSTRACT Photothermal ablation (PTA) therapy has a great potential to revolutionize conventional therapeutic approaches for cancers, but it has been limited by difficulties in obtaining biocompatible photothermal agents that have low cost, small size (<100 nm), and high photothermal conversion efficiency. Herein, we have developed hydrophilic plate-like Cu_9S_5 nanocrystals (NCs, a mean size of ~70 nm × 13 nm) as a new photothermal agent, which are synthesized by combining a thermal decomposition and ligand exchange route. The aqueous dispersion of as-synthesized Cu_9S_5 NCs exhibits an enhanced absorption (*e.g.*, ~1.2×10^9 M^{-1} cm^{-1} at 980 nm) with the increase of wavelength in near-infrared (NIR) region, which should be attributed to localized surface plasmon resonances (SPR) arising from p-type carriers. The exposure of the aqueous dispersion of Cu_9S_5 NCs (40 ppm) to 980 nm laser with a power density of 0.51 W/cm^2 can elevate its temperature by 15.1 °C in 7 min; a 980 nm laser heat conversion efficiency reaches as high as 25.7%, which is higher than that of the as-synthesized Au nanorods (23.7% from 980 nm laser) and the recently reported $Cu_{2-x}Se$ NCs (22% from 808 nm laser). Importantly, under the irradiation of 980 nm laser with the conservative and safe power density over a short period (~10 min), cancer cells *in vivo* can be efficiently killed by the photothermal effects of the Cu_9S_5 NCs. The present finding demonstrates the promising application of the Cu_9S_5 NCs as an ideal photothermal agent in the PTA of *in vivo* tumor tissues.

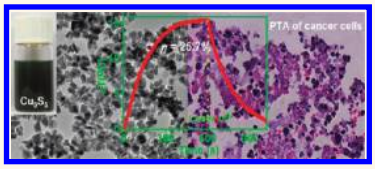

KEYWORDS: hydrophilic Cu_9S_5 nanocrystals · photothermal conversion · 980 nm laser · thermal therapy · heat conversion efficiency

Conventional therapeutic approaches for treatments and cure of cancers include surgery, radiation therapy, chemotherapy, hormone therapy immunotherapy, *etc.*, but they have many disadvantages, such as harming healthy cells, destroying the immune system, and resulting in an increased incidence of second cancers.[1,2] Recently, as a minimally invasive and potentially effective treatment alternative to conventional approaches, photothermal ablation (PTA) therapy has attracted much interest.[3−6] In particular, near-infrared (NIR, λ = 700−1100 nm) laser-induced PTA has received increasing attention because the NIR laser is absorbed less by biological tissues and the typical penetration depth of the NIR (such as 980 nm) light can reach several centimeters in biological tissues.[7−9] When applying the NIR laser to treat cancer tissues, in order to promote the photothermal conversion efficiency and particularly improve lasers' discrimination for the PTA of the targeted cancers, photothermal agents which can convert the NIR light energy into thermal energy are generally indispensable. Thus, it is very important that the advancement of the NIR photothermal cancer therapy is dependent on the development of photothermal agents.

Currently, there have been chiefly four types of photothermal agents. The first type is the organic compounds such as indocyanine green (ICG) dye[9] and polyaniline nanoparticles,[3] which suffer from serious photobleaching or low photothermal conversion efficiency. The second type is carbon-based materials, including carbon nanotubes (CNT),[4,10−17] graphene oxide,[18] and reduced graphene oxide.[19] The third type is metal nanostructures, including Ge nanoparticles,[20] Pd nanosheets,[21−23] and Au nanostructures (supramolecularly assembled nanoparticles,[24−27] nanorods,[28−31] nanoshells,[32−34] hollow nanospheres,[35−38] nanocages,[39−41] and nanocrosses[42]). These metal nanostructures exhibit the intense absorption with a maximum molar extinction coefficient of 10^8−10^{11} M^{-1} cm^{-1} and

* Address correspondence to hu.junqing@dhu.edu.cn.

Received for review August 25, 2011 and accepted November 7, 2011.

Published online November 07, 2011
10.1021/nn203293t

relatively high photothermal conversion efficiency (*e.g.*, Au nanoshells (13%) and nanorods (21%) irradiated with 800 nm light[43]), due to their tunable surface plasmon resonance (SPR) properties, and they have appeared as the most studied agents for the NIR photothermal therapy. However, these noble-metal-based nanostructures are too expensive to limit their wide applications. The last type recently is copper chalcogenide semiconductors, including CuS[6,44,45] and $Cu_{2-x}Se$[43] NCs, which are new kinds of promising photothermal agents due to their low cost and low cytotoxicity.

Although copper chalcogenide semiconductors have a great potential for use as photothermal agents, one of the limitations is their unsatisfied photothermal conversion efficiency.[44] For example, when CuS nanoparticles with a size of ~3 nm serve as the photothermal agent, the power intensity of the 808 nm laser required to cause sufficient cell death is as high as 16 and 24 W/cm^2 and ~48 and 72 times higher than the conservative limit (~0.33 W/cm^2) of this laser intensity setting for human skin exposure.[44,45] Very recently, we reported the synthesis of CuS flower-like superstructures with a mean size of ~1 μm as an efficient 980 nm laser-driven photothermal agent.[6] Under the irradiation of the 980 nm laser with a low power density of 0.51 W cm^{-2} (the conservative limit of 980 nm laser intensity setting for human skin exposure is ~0.726 W/cm^2),[7] both cancer cells packaged by chicken skin and *in vivo* can be efficiently killed due to the photothermal effects of CuS superstructures over a short period (5−10 min). It should be noted that the size (~1 μm) of the CuS superstructures in our case is too large, probably a result that the potential as photothermal agent in biological applications is significantly limited. Unfortunately, if the size of CuS materials decreases, the photothermal conversion efficiency will be reduced dramatically.[45] Thus, it should develop new copper chalcogenide semiconductors with a small size (<100 nm) but high photothermal conversion efficiency to meet the demand of biological applications.

Herein, we report the development of hydrophilic Cu_9S_5 plate-like nanocrystals with a mean size of ~70 nm × 13 nm, which are synthesized by combining a simple modified thermal decomposition (from a single molecular precursor) and ligand exchange route, as a novel photothermal agent with the 980 nm laser heat photothermal conversion efficiency up to 25.7% for highly effective photothermal ablation of cancer cells *in vivo*. Such a high photothermal conversion efficiency that Cu_9S_5 NCs exhibit is due to the localized surface plasmon resonances arising from p-type carriers in vacancy-doped NCs and higher than that of the as-synthesized Au nanorods (23.7% from 980 nm laser) and the recently reported $Cu_{2-x}Se$ NCs (22% from 808 nm laser).

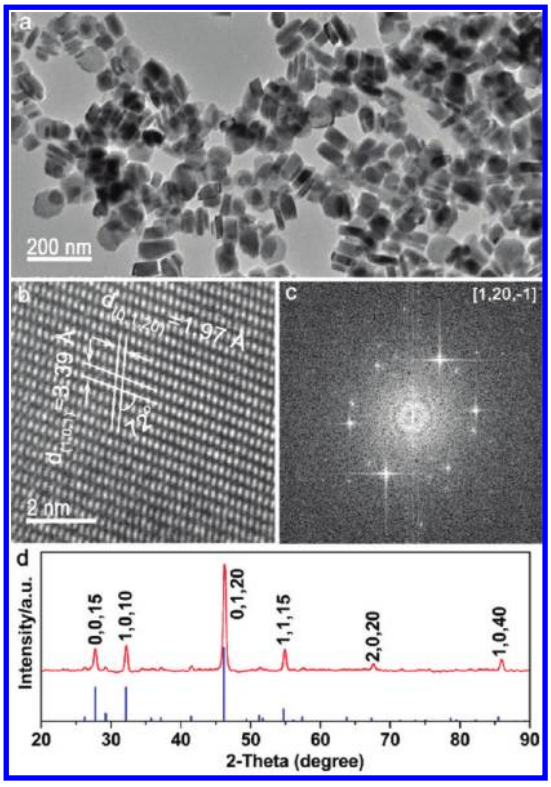

Figure 1. (a) Low-magnification, (b) HRTEM images of the synthesized Cu_9S_5 NCs, (c) corresponding FFT diffraction pattern from the image in (b). (d) XRD patterns of the as-prepared product (red line) and the standard Cu_9S_5 powders (blue bar) on a JCPDS card (no. 47-1748).

RESULTS AND DISCUSSION

Synthesis and Characterization of Cu_9S_5 Nanocrystals. Hydrophobic Cu_9S_5 nanocrystals capped with oleylamine ligands were prepared by a simple modified thermal decomposition route from a single molecular precursor. Figure 1a shows a representative TEM image of the as-prepared NC samples. The obtained Cu_9S_5 NCs display slightly irregular and plate-like morphology with an average diameter of 70 and an average thickness of ~13 nm. Further investigation of microstructure information of the as-obtained Cu_9S_5 NCs is carried out by high-resolution TEM (HRTEM) image and electron diffraction (ED) pattern. A HRTEM image (Figure 1b) shows a single crystal with resolved interplanar *d*-spacings of ~0.339 and 0.197 nm, corresponding to the (1, 0, 1) and (0, 1, 20) lattice fringes of a rhombohedral phase of Cu_9S_5 single crystal, respectively. The diffraction pattern is shown in Figure 1c, which is obtained from the fast Fourier transform (FFT) from the HRTEM image in Figure 1b and can be indexed to the [1, 20, −1] zone axis of the rhombohedral structure of the Cu_9S_5 crystal. Figure 1d shows the XRD patterns (top curve) of these Cu_9S_5 NCs and the standard Cu_9S_5 powders on the JCPDS card (no. 47-1748). The well-defined peaks in this pattern indicate the formation of pure rhombohedral phase of Cu_9S_5 with high crystallinity. The cell constants of Cu_9S_5 are calculated to be

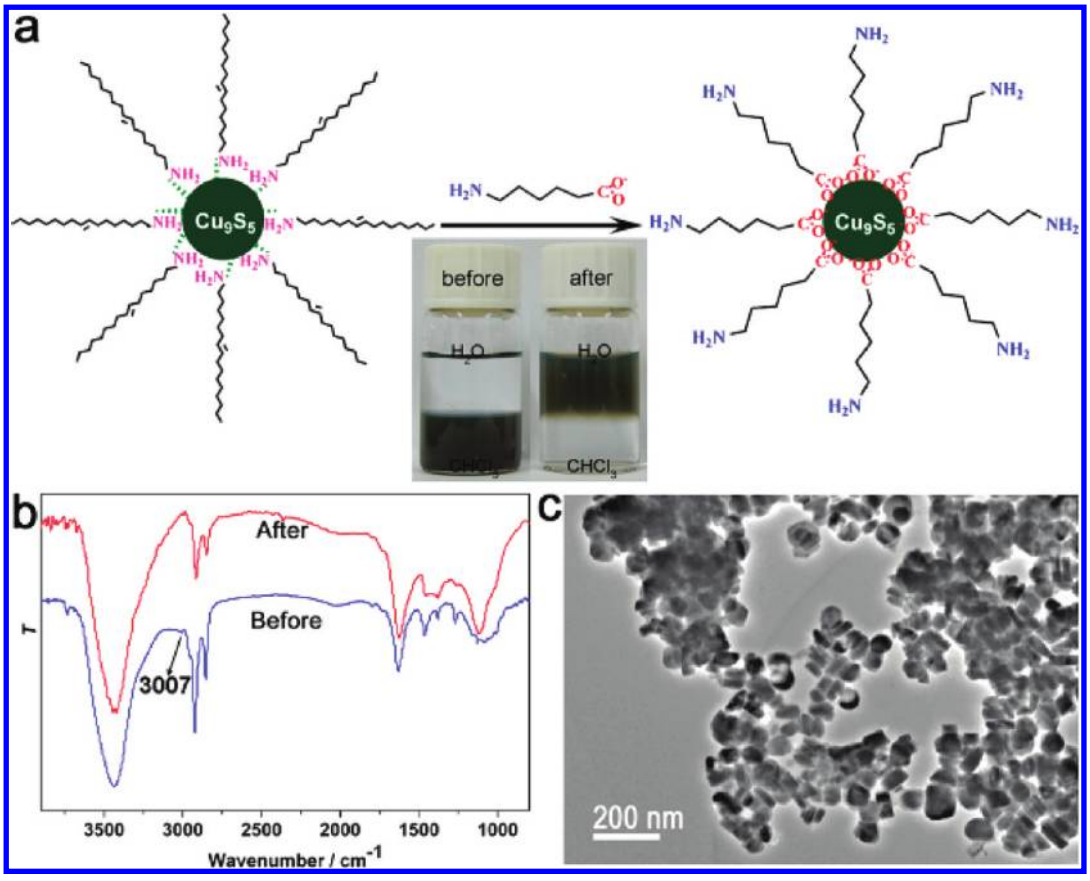

Figure 2. (a) Schematic illustration of the preparation of the hydrophilic Cu_9S_5 NCs *via* ligand exchange. Inset of the photo showing the Cu_9S_5 NCs dispersed into different solvents (H_2O and $CHCl_3$) before and after the ligands' exchange. (b) FTIR spectra of the Cu_9S_5 NCs before (blue line) and after (red line) ligands' exchange. (c) TEM image of the as-prepared hydrophilic Cu_9S_5 NCs.

$a = b = 3.93$ and $c = 48.11$ Å, which agree well with the data obtained from the JCPDS card.

To obtain hydrophilic Cu_9S_5 NCs for biological applications, a ligand exchange method was used to modify the surface property of the Cu_9S_5 NCs, as schematically shown in the Figure 2a, where oleylamine ligands capped on the surface of Cu_9S_5 NCs were exchanged by 6-amino caproic acid (ACA). A middle-lower inset shows the photo of the Cu_9S_5 NCs dispersed into different solvents (H_2O and $CHCl_3$) before and after the ligands' exchange. It can be seen that as-synthesized hydrophobic Cu_9S_5 NCs capped with OM ligands can easily be dispersed into a nonpolar solvent such as $CHCl_3$ (left photo of the inset), and the ligands' exchange by replacing OM with 6-ACA ligands results in the formation of hydrophilic Cu_9S_5 NCs and their high solubility in water (right photo of the inset). Also, the capping ligands on the surface of the Cu_9S_5 NCs before and after treatment with the 6-ACA are identified by the Fourier transform infrared (FTIR) spectra (Figure 2b). In both samples before and after the ligands' exchange, a broad band at around 3450 cm^{-1} corresponds to N—H and/or O—H stretching vibration;[46] the transmission bands at 2924 and 2854 cm^{-1} are, respectively, assigned to the asymmetric (ν_{as}) and symmetric (ν_s) stretching vibrations of methylene (CH_2) in the long alkyl chain; in addition, two bands at 1634 and 1384 cm^{-1} are attributed to N—H bending and C—N stretching modes, respectively.[47,48] However, by comparison of the spectra before the ligands' exchange, a peak at 3007 cm^{-1} due to the C═C—H stretching vibration can clearly be seen (blue line),[49] whereas this featured peak apparently disappears in the spectrum after the ligands' exchange (red line), suggesting that the OM ligands are replaced by 6-ACA ligands. These results indicate that the hydrophobic Cu_9S_5 NCs have been successfully transferred into hydrophilic ones by the ligands' exchange. Figure 2c presents a representative TEM image of the hydrophilic Cu_9S_5 NCs after the ligands' exchange. It shows that the hydrophilic sample consists primarily of nanoplates and has no obvious morphological change, compared with the hydrophobic sample before the ligands' exchange (Figure 1a).

As a result of the presence of the ACA ligands on the surface of hydrophilic Cu_9S_5 NCs, the aqueous dispersion of Cu_9S_5 NCs has high stability and even can remain unchanged after being dispersed in water for 1 week (the inset of Figure 3). The optical property of the aqueous dispersion containing 40 ppm of the

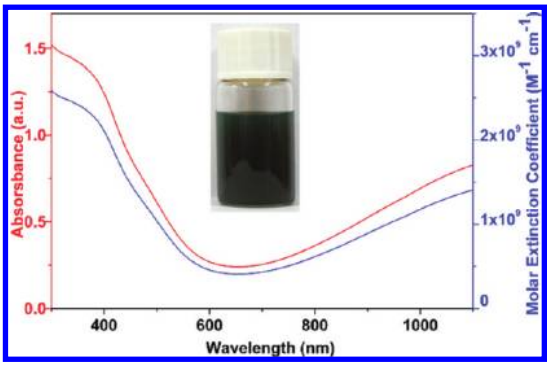

Figure 3. Absorption spectrum (red line) and molar extinction coefficient (blue line) of the aqueous dispersion of hydrophilic Cu_9S_5 NCs (40 ppm). An inset photograph shows the hydrophilic Cu_9S_5 NCs in water after 1 week.

Cu_9S_5 NCs was examined by using UV−vis−NIR spectroscopy (Figure 3, red line). The spectrum is similar to what has been reported previously for the Cu_9S_5 NCs[50] and exhibits the short-wavelength absorption edged at ~620 nm and a minimum of around 650 nm, which agrees well with the reported band gap (E_g = 1.57 eV) of the Cu_9S_5 material. Importantly, Cu_9S_5 NCs show an increased absorption with the increase of wavelength in the NIR region (λ = 650−1100 nm). The NIR absorbance of the as-synthesized Cu_9S_5 NCs is mainly attributed to the localized surface plasmon resonances (SPR) because that Cu_9S_5 is a p-type semiconductor with a relatively high carrier (holes) concentration and exhibits a strong free carrier absorption, as demonstrated by Burda *et al.*[50] and Alivisatos *et al.*[51] Additionally, Cu_9S_5 (or $Cu_{1.8}S$) is an intermediate phase of copper sulfides ($Cu_{2-x}S$, $0 \le x \le 1$) (*i.e.*, $x = 0.2$) and has many Cu deficiencies which vary with conditions used for their synthesis. Our one-pot thermal decomposition route resulted in the formation of Cu_9S_5 NCs, and the Cu deficiencies within these NCs exhibited NIR absorbance peaks. However, very recently, Alivisatos *et al.*[51] have revealed that the $Cu_{2-x}S$ NCs with vacancy concentrations of ~10^{21} cm^{-3} demonstrate surface plasmon resonance bands, thus confirming that substoichiometric copper(I) chalcogenides (*e.g.*, Cu_9S_5) have absorption characteristics similar to those of metals.[51]

To compare the NIR photoabsorption capability of the Cu_9S_5 NCs with that of the reported photothermal agents (such as Au and $Cu_{2-x}Se$), the extinction coefficient ε (λ) of the Cu_9S_5 NCs is given, according to eq 1[50] (see the Supporting Information part 1 for the detailed calculations)

$$\varepsilon = (AV_{NC}\rho N_A)/(LC_{wt}) \quad (1)$$

where ε is the molar extinction coefficient, A is the absorbance at a wavelength λ, V_{NC} (in cm^3) is the average volume of the NCs, ρ is the density of the NCs assuming that it is the same as bulk material, N_A is Avogadro's constant, L is the path length (1 cm), and C_{wt} (in g/L) is the weight concentration of the NCs.

On the basis of the TEM observations, we assume that the average volume for individual Cu_9S_5 NC is ~2.02×10^{-17} cm^3 (Figure S1). In addition, the density ρ for Cu_9S_5 is about 5.6 g/cm^3. So, the obtained extinction coefficients $\varepsilon(\lambda)$ from the measured absorbance A of the Cu_9S_5 NCs is shown in Figure 3 (blue line). It is clear that the Cu_9S_5 NCs exhibit high molar extinction coefficients, for example, ~1.2×10^9 M^{-1} cm^{-1} at 980 nm, which is higher than that of CNTs (r = 0.6 nm, L = 150 nm, ~7.9×10^6 at 808 nm[52]), $Cu_{2-x}Se$ (~7.7×10^7 M^{-1} cm^{-1} at 980 nm[43]) but is lower than that of Au nanostructures (*e.g.*, Au nanorods, r = 5 nm, L = 27 nm, ~1.9×10^9 at 650 nm;[53] Au nanoshells, r_1 = 55 nm, r_2 = 65 nm, ~2×10^{11} at 800 nm[54]). The high molar extinction coefficients measured for the present Cu_9S_5 NCs are also consistent with plasmon absorption[51] and are orders of magnitude higher than expected for an indirect optical transition and considerably higher than strongly absorbing organic dyes, direct band gap semiconductor quantum dots.[43]

Photothermal Conversion Performance of the Cu_9S_5 Nanocrystals. The strong SPR absorption of as-synthesized Cu_9S_5 NCs in the NIR region motivates us to investigate the potential of these Cu_9S_5 NCs in photothermal cancer therapy using a 980 nm laser at the plasmon band. We extensively examined the temperature elevation of pure water (a control experiment) and aqueous dispersions containing Cu_9S_5 NCs with different concentrations under the irradiation of 980 nm laser with a power density of 0.51 W/cm^2, as shown in the Figure 4a. The control experiment of pure water (*i.e.*, without a Cu_9S_5 NC) demonstrates that the temperature of the pure water is only increased by less than 2.2 °C from the room temperature of 25 °C in 7 min, as suggested by a bottom curve in Figure 4a. With the increase of the concentration of the Cu_9S_5 NCs (*i.e.*, 1.2, 2.5, 5.0, 10, 20, and 40 ppm), the temperature of the aqueous dispersion of the Cu_9S_5 NCs can increase by 6.8−15.1 °C in 7 min, as shown by six top curves in Figure 4a, respectively, indicating that the Cu_9S_5 NCs can rapidly and efficiently convert the 980 nm laser energy into thermal energy. As shown in Figure 4b, the temperature change (ΔT) in 7 min, which is calculated from the Figure 4a, goes up dramatically with the concentration of Cu_9S_5 NCs increasing to 5 ppm, and then exhibits a fairly flat line upon the concentration of Cu_9S_5 NCs further increasing to 40 ppm. This phenomenon should be attributed to a fast heat loss at relatively high temperature.

The photothermal conversion efficiency of the Cu_9S_5 NCs was measured by a modified method similar to the report by Roper *et al.*[55] The temperature change of the aqueous dispersion of the Cu_9S_5 NCs (40 ppm) was recorded as a function of time under continuous

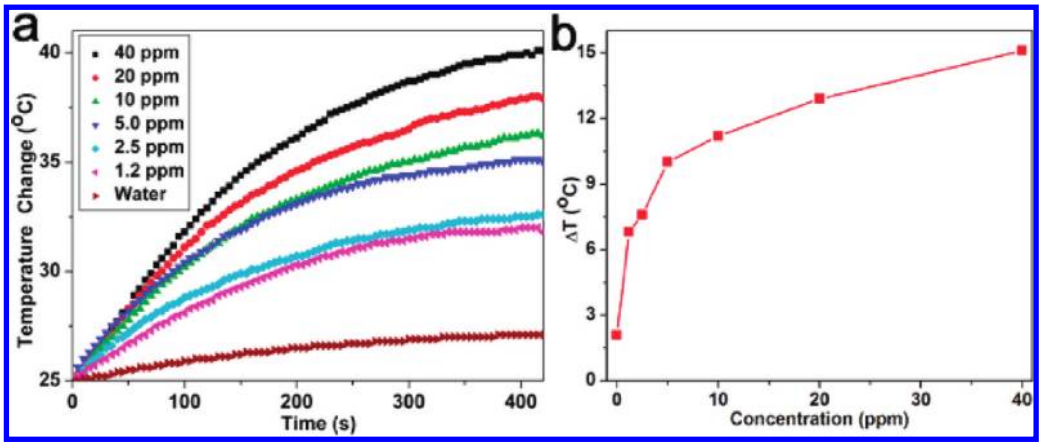

Figure 4. (a) Temperature elevation of the pure water and the aqueous dispersion of Cu_9S_5 NCs with different concentrations (1.2, 2.5, 5.0, 10, 20, and 40 ppm) as a function of irradiation time (0−7 min). Pure water was used as a control, and room temperature was 25 °C. (b) Plot of temperature change (ΔT) over a period of 7 min *versus* the concentration of the Cu_9S_5 NCs' aqueous dispersion.

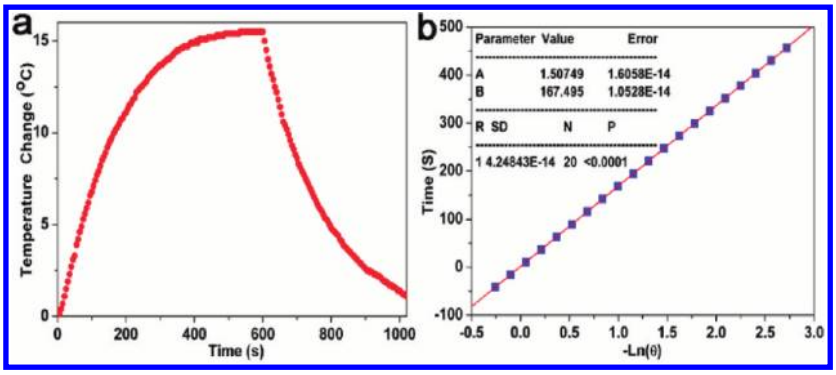

Figure 5. (a) Photothermal effect of the irradiation of the aqueous dispersion of Cu_9S_5 NCs (40 ppm) with the NIR laser (980 nm, 0.51 W/cm^2), in which the irradiation lasted for 10 min, and then the laser was shut off. (b) Time constant for heat transfer from the system is determined to be τ_s = 167 s by applying the linear time data from the cooling period (after 420 s) *versus* negative natural logarithm of driving force temperature, which is obtained from the cooling stage of panel a.

irradiation of 980 nm laser with a power density of 0.51 W/cm^2, until steady state temperature was reached (Figure 5a). It was found that the aqueous dispersion of the Cu_9S_5 NCs (40 ppm) exhibits the highest temperature elevation of 15.1 °C under the irradiation for 10 min, and its temperature remains invariant with time extending. Subsequently, 980 nm laser as the irradiation source was shut off, and the temperature decrease of the aqueous dispersion was monitored to determine the rate of heat transfer from the dispersion system to the environment (Figure 5a).

Following Roper's report,[55] the photothermal conversion efficiency, η, was calculated using the following eq 2 (see the Supporting Information part 2 for the detailed calculations)

$$\eta = \frac{hS(T_{max} - T_{surr}) - Q_{dis}}{I(1 - 10^{-A_{980}})} \quad (2)$$

where h is heat transfer coefficient, S is the surface area of the container, and the value of hS is obtained from the Figure 5b. The T_{max} is the equilibrium temperature, T_{surr} is ambient temperature of the surroundings, and ($T_{max} - T_{surr}$) was 15.1 °C according to Figure 5a. The Q_{dis} expresses heat dissipated from light absorbed by the quartz sample cell itself, and it was measured independently to be 10.9 mW using a quartz cuvette cell containing pure water without a NC. I is incident laser power (0.51 mW/cm^2), A_{980} is the absorbance (0.6581) of Cu_9S_5 NCs at 980 nm (Figure S2). Thus, the 980 nm laser heat conversion efficiency (η) of the Cu_9S_5 NCs can be calculated to be 25.7%. In fact, the calculation procedure of η is independent of the shape of the Cu_9S_5 NCs and concentration of the Cu_9S_5 NCs' aqueous dispersion. Compared with the previous heat conversion efficiency of the $Cu_{2-x}Se$ NCs (22%) under the irradiation of 808 nm laser,[43] this heat conversion efficiency of the Cu_9S_5 NCs is the higher, which should be attributed to the strong NIR absorption and effective nonradiative electron relaxation dynamics.[56]

In order to further compare the Cu_9S_5 NCs with other materials (*e.g.*, Au nanorods), we have measured the photothermal conversion efficiency of the Cu_9S_5 NCs and Au nanorods at the same experimental conditions, thus the photothermal conversion efficiencies

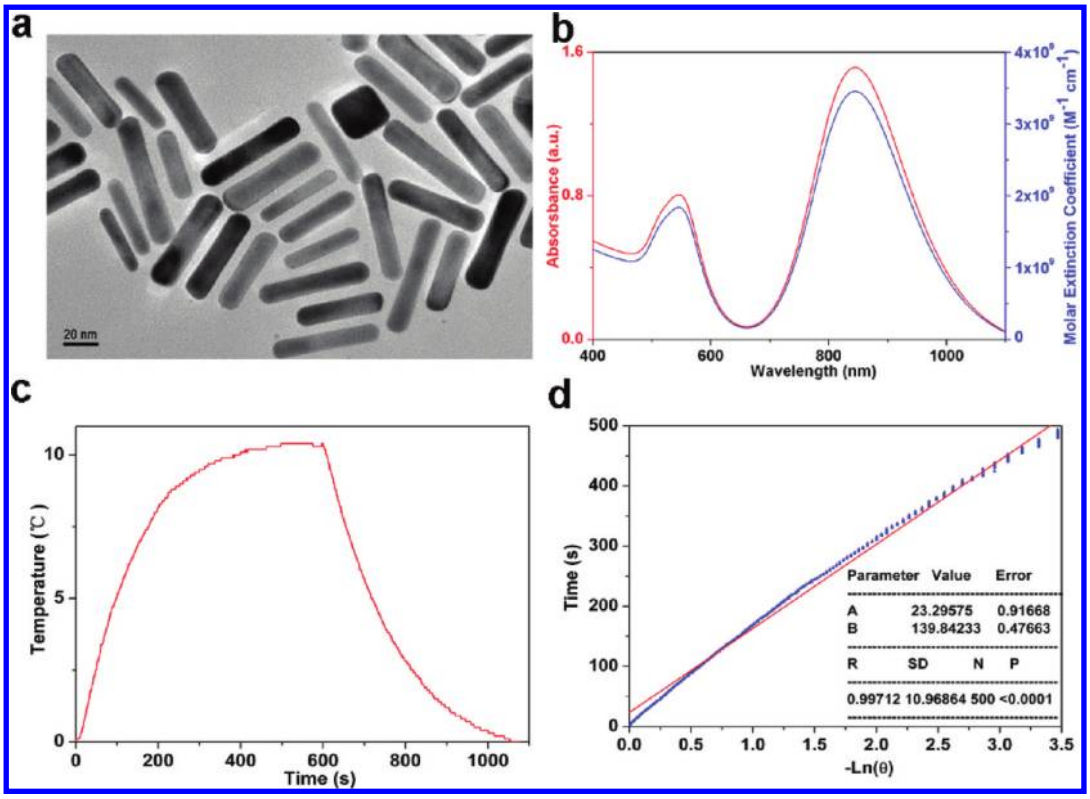

Figure 6. (a) TEM image. (b) Absorption spectrum (red line) and molar extinction coefficient (blue line) of the aqueous dispersion of the synthesized Au nanorods (40 ppm). (c) Photothermal effect of the aqueous dispersion of the Au nanorods (40 ppm) irradiated with 980 laser (a power density of 0.51 W/cm^2), in which the irradiation lasted for 10 min, and then the laser was shut off. (d) Time constant for heat transfer from the system is determined to be τ_s = 140 s by applying the linear time data from the cooling period (after 500 s) *versus* negative natural logarithm of driving force temperature, which is obtained from the cooling stage of panel c.

of them are comparable. TEM image (Figure 6a) shows that as-synthesized Au nanorods[57] have an average size of 50 × 15 nm. An absorption spectrum (Figure 6b, red line) suggests that the longitudinal plasmon wavelength of the synthesized Au nanorods (dispersed in water) is centered at ~845 nm. On the basis of this absorption spectrum, the molar extinction coefficient (Figure 6b, blue line) is calculated by the above eq 1[50] to be ~1.1 × 10^9 M^{-1} cm^{-1} at 980 nm, which is similar with the previous reports.[53] According the data obtained from the Figure 6c,d, the 980 nm laser heat conversion efficiency (η) of the as-synthesized Au nanorods is further calculated by the above eq 2[53] to be 23.7%, which is much lower than that of the reported Au nanorods (60[58] and 90%[57]) obtained at different measurement conditions but is nearly equivalent to that of the present Cu_9S_5 NCs (25.7%). So, the photothermal conversion efficiency of the as-synthesized Cu_9S_5 NCs (25.7%) can be comparable to the reported values for Au nanorods under the measurement conditions.

The fact that the photothermal conversion efficiency of the Cu_9S_5 NCs is nearly equivalent to that of these Au nanorods is mainly due to the similar NIR absorption at 980 nm. Wang *et al.*[57] have studied the effect of the plasmon wavelength on the photothermal conversion of the Au nanostructures. It is found that the dispersion of Au nanoparticles will reach the highest temperature when the plasmon resonance wavelength is equal to the illumination laser wavelength, which means that the stronger the absorbance at the illumination laser wavelength, the higher the temperature of the photothermal materials. In our experiment, the absorption of these Cu_9S_5 NCs and the Au nanorods at 980 nm, in which the continuous semiconductor diode laser was used for their measurement, is found to be ~1.2 × 10^9 and 1.1 × 10^9 M^{-1} cm^{-1}, respectively, and thus is similar. The similar NIR absorption at 980 nm of the Cu_9S_5 NCs and the Au nanorods results in that they have nearly the same photothermal conversion efficiency in our study.

Applications As Photothermal Agents. The ideal photothermal agents should be nontoxic or low-toxic for biological applications. To evaluate the cytotoxicity of the Cu_9S_5 NCs, a 3-(4,5-dimethylthiazol-2-yl)-2,5-diphenyltetrazolium bromide (MTT) assay with the human cervical carcinoma cell line HeLa was used. To examine the effect of the copper ions released from the Cu_9S_5 NCs to solution on cells, the concentration of the released copper ions in the solution and comparable cytotoxicity of $CuCl_2$ solution were investigated. The cytotoxicity of $CuCl_2$ was measured with the same

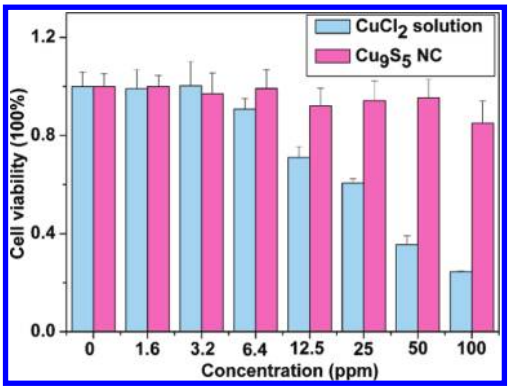

Figure 7. Cell viabilities were estimated by the MTT proliferation tests *versus* incubation concentrations (0−100 ppm) of the solutions of $CuCl_2$ and Cu_9S_5 NCs. Cells were incubated with the solutions of $CuCl_2$ and Cu_9S_5 NCs at 37 °C for 24 h.

procedure as that of the Cu_9S_5 NCs. In order to obtain the concentration of the released copper ions (from Cu_9S_5 NCs) in the solution, 10 mL of DMEM (Dulbecco's modified Eagle's medium, which contains 10% fetal bovin serum, 4 mM glutamine, 100 U/mL penicillin, 100 mg/mL streptomycin, and 1% HEPES (hydroxyethyl piperazine ethanesulfonic acid)) solution consisting of Cu_9S_5 NCs with a concentration of 100 ppm, was incubated for 24 h at 37 °C in the presence of 5% CO_2; then the Cu_9S_5 NCs were removed by centrifuging (14000 rpm for 10 min), and the supernatant solution was further purified by centrifuging two times; the content of copper irons in the supernatant solution was determined by the inductively coupled plasma atomic emission spectroscopy (ICP-AES). The supernatant solution of the copper irons was incubated in digestion solution containing a mixed acid (made of nitric acid and perchloric acid with a volume ratio of 4:1) for 4 h.[59] In order to get a reliable result, the measurements of the content of the released copper irons and the cytotoxicity of the solutions of the Cu_9S_5 NCs and $CuCl_2$ were both carried out in parallel three times and the average values are shown in the Figure 7. It can be seen that $CuCl_2$ solution, the original source material for the preparation of Cu_9S_5 NCs, was significantly more cytotoxic than that of the Cu_9S_5 NCs' solution. Almost 60% of the cells were dead after treatment with the $CuCl_2$ solution at a concentration as low as 50 ppm, while no significant differences in the proliferation of the cells were observed in the presence of Cu_9S_5 NCs with concentrations of 1.6−100 ppm, and the cellular viability was estimated to be higher than 80% after 24 h. Considering that the content of copper irons released from the Cu_9S_5 NCs (100 ppm) in the MEM solution (containing 1% HEPES) after 24 h is only 3.7 ppm, the lower cytotoxicity of the Cu_9S_5 NCs' solution, compared with the $CuCl_2$ solution, should be attributed to the better stability in the DMEM solutions. So, it is believed that the solutions of the Cu_9S_5 NCs with a much more low concentration (*e.g.*, 1.6, 3.2, 6.3, 12.5, 25, and 50) (<100) can be considered to have a very low cytotoxicity.

The photothermal conversion efficiency of these Cu_9S_5 NCs as photothermal agents to destroy the cancer cells was evaluated *in vivo*. Severe combined immunodeficiency mice (SCID) were inoculated subcutaneously with 2×10^6 PC-3 cells in the side of the rear leg 21 days before the irradiation treatment experiment (Figure S3). When the tumors inside the SCID grew to 5−10 mm in a diameter, the SCID mice were randomly allocated into treatment and control groups. The SCID mice in the treatment group were injected with 100 μL of the Cu_9S_5 NCs' aqueous dispersion (40 ppm) at the central region of the tumor with a depth of ~4 mm, while the SCID mice in the control group were injected with water. After 1 h, the tumors inside the SCID mice from both the treatment and control groups were irradiated with 980 nm laser at 0.51 W/cm^2 for 10 min. The photographs of the experimental setup and the heat treatment on the cancerous tissue are shown in Figure S4. After intratumoral injection with Cu_9S_5 NCs' aqueous dispersion or water and then the laser irradiation, the photothermal conversion efficiency of these Cu_9S_5 NCs as photothermal agents to destroy the cancer cells is evaluated in detail according to the cell shape changes (*e.g.*, cell shrinkage, extraordinary cytoplasmic eosinophilia, clear cell change, and cytoplasmic vacuolization), nuclear changes (*e.g.*, nucleomegaly, multinucleation, hyperchromasia, and symplastic changes), and coagulative necrosis. Detailed and clear microscopic pictures showing histological examination of tumors are given in Figure 8 (more pictures with a different magnification are also been shown in Figures S5 and S6 in Supporting Information). The histopathological analysis of the specimens of the control group (Figure 8a,b) shows that no differences regarding the cells' size and shape, nuclear modifications, or necrosis after irradiation occur. It suggests that the heat of pure water converted from the 980 nm laser irradiation, which is only increased by less than 2.2 °C (Figure 4a), is not enough to kill the cancer cells. The representative histopathological images of the treatment group are shown in the Figure 8c,d. Clearly, the common signs due to thermal cell necrosis are presented on most areas of the examined tumor slide in the entire tumor mass (Figure 8c); more details, such as malignant cells shrunken, loss of contact, eosinophilic cytoplasm, and nuclear damage (pyknotic and fragmentized nuclei), can be obvious in Figure 8d. In addition, thermal injury has also been observed in the stromal reactive tissue as the destruction of the tumor cells. For example, the connective tissue surrounding the tumor cells was disrupted with fragmented collagen fibers (Figure S6). Also, the distribution of the Cu_9S_5 NCs in the tumor after irradiation by the 980 nm has been examined by field emission scanning electron microscope (SEM)

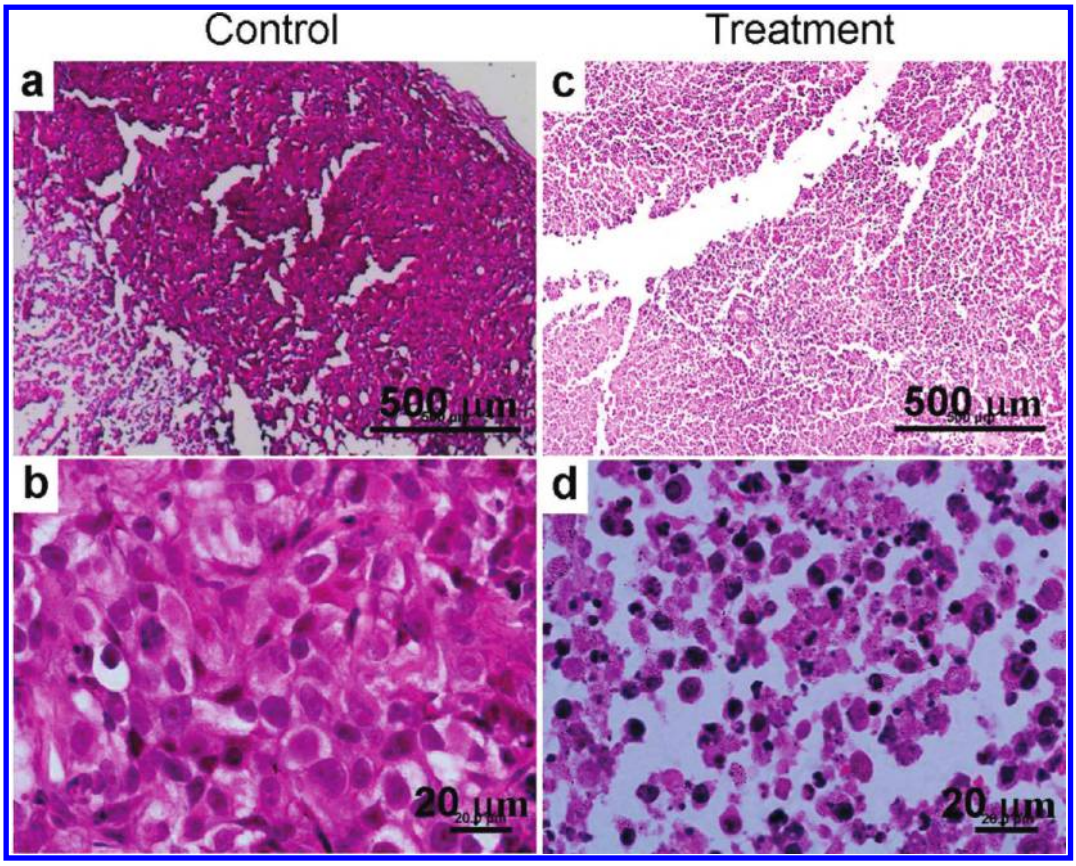

Figure 8. (a−d) Representative H&E stained histological images of *ex vivo* tumor sections treated by the irradiation of 980 nm laser with the power density of 0.51 W/cm^2 over a period of 10 min injected with (a,b) water, (c,d) aqueous dispersion (40 ppm) of the Cu_9S_5 NCs.

(Figure S7; see the SEM sample preparation in the Supporting Information). Clearly, the Cu_9S_5 NCs are homogeneously distributed on the tumor from the treatment group, which the size and shape are both well preserved, as suggested by TEM images (Figure 1a), and no aggregation areas of the Cu_9S_5 NCs have been observed on the tumor in our careful SEM imaging (Figure S7c). Therefore, the Cu_9S_5 NCs have great potential as an ideal photothermal agent for the PTA of specific targets such as *in vivo* tumor tissues. To the best of our knowledge, this is the first time that the PTA of cancer cells *in vivo* was realized by using Cu_9S_5 NCs irradiated with 980 nm laser with a low and safe power density (0.51 W/cm^2).

CONCLUSION

In summary, hydrophilic Cu_9S_5 NCs with a mean size of ~70 nm × 13 nm as a novel photothermal agent have been prepared by a simple thermal decomposition route and subsequent ligand exchange process. The aqueous dispersion of the Cu_9S_5 NCs (40 ppm) exhibits an intense absorbance in the near-IR region (650−1100 nm), and its temperature can be increased by 15.1 °C in 7 min under the irradiation of 980 nm laser with a power density of 0.51 W/cm^2 due to the effective photothermal conversion. The photothermal conversion efficiency of the Cu_9S_5 NCs can be as high as 25.7%, which is higher than that of the as-synthesized Au nanorods and the recently reported $Cu_{2-x}Se$ NCs. Importantly, cancer cells *in vivo* can be efficiently killed by the photothermal effects, which are realized by a very low concentration (40 ppm) aqueous dispersion of the Cu_9S_5 NCs under the irradiation of 980 nm laser with a low and safe power density of 0.51 W/cm^2. Therefore, these Cu_9S_5 NCs have a great superiority as a new photothermal agent for the NIR-induced PTA of cancer, due to their small size (<100 nm) and high photothermal conversion efficiency, as well as their low cost and low cytotoxicity.

EXPERIMENTAL SECTION

Synthesis of Cu_9S_5 Nanocrystals and Au Nanorods. *Synthesis of Copper Diethyldithiocarbamate Precursor.* All of the chemicals were bought from Sinopharm Chemical Reagent Co. China and are analytically pure and were used as received without further purification. Copper diethyldithiocarbamate [Cu(DEDTC)$_2$] precursor was prepared by reacting $CuCl_2 \cdot 2H_2O$ with sodium diethyldithiocarbamate (SDEDTC) as follows: A solution of

SDEDTC (10 mmol) in distilled water (5 mL) was added into another solution containing $CuCl_2$ (10 mmol) and distilled water (10 mL) under magnetic stirring, forming a dark brown turbid solution. Then, the dark brown turbid solution was kept for 1 h of stirring. Lastly, the dark brown $Cu(DEDTC)_2$ precursor was obtained by filtration and dried at room temperature under vacuum before use.

Synthesis of Oleylamine-Capped Cu_9S_5 NCs. Cu_9S_5 NCs were prepared by a modified thermal decomposition process, as described eleswhere.[60] In a typical procedure, 15 mL of oleylamine (OM) was slowly heated to 300 °C in a flask under magnetic stirring for 30 min to remove residual water and oxygen in which the flask was purged periodically with dry nitrogen gas. Then, another 5 mL of OM containing 1 mmol $Cu(DEDTC)_2$ was injected into the above hot OM, and the resulting solution became dark green immediately. After keeping the temperature for 10 min, the resulting solution was cooled to 60 °C naturally. An addition of ethanol (30 mL) to the reaction mixture afforded a black product by centrifuging, and the precipitates were then washed twice with ethanol and further purified by dispersing in 5 mL of chloroform and then precipitated with excess ethanol.

Ligand Exchange with 6-Amino Caproic Acid. A solution of 6-amino caproic acid (ACA) (1 mmol) and equivalent $NH_3 \cdot H_2O$ in 5 mL of distilled water was added into another solution containing OM-capped Cu_9S_5 NCs (0.1 g), ethanol (30 mL), distilled water (10 mL), and hexane (35 mL), under magnetic stirring, forming a dark green solution. Then, the dark green solution was heated to 70 °C and kept at this temperature for 4 h. When the reaction was finished, the Cu_9S_5 NCs were transferred to an aqueous phase from an organic phase. Then, the hydrophilic Cu_9S_5 NCs were collected by centrifuging, and the precipitates were then washed twice with ethanol. Finally, the hydrophilic Cu_9S_5 NCs were dispersed again in water for later use.

Synthesis of Au Nanorods. Au nanorods were grown using the silver ion-assisted seed-mediated method, by referring to the previous literature.[57] Typically, the seed solution was prepared by the addition of $HAuCl_4$ (0.01 M, 0.25 mL) into cetyltrimethylammonium bromide (CTAB, 0.1 M, 10 mL) in one plastic tube (15 mL) with gentle mixing. A freshly prepared, ice-cold $NaBH_4$ solution (0.01 M, 0.6 mL) was then injected into the mixture solution, followed by rapid inversion for 2 min. The seed solution was kept at room temperature for at least 2 h before use. To grow Au nanorods, $HAuCl_4$ (0.01 M, 2.0 mL) and $AgNO_3$ (0.01 M, 0.4 mL) were mixed with CTAB (0.1 M, 40 mL) in another plastic tube (50 mL). HCl (1.0 M, 0.8 mL) was then added to adjust the pH of the solution to 1−2, followed by the addition of ascorbic acid (0.1 M, 0.32 mL). Finally, the seed solution (0.096 mL) was injected into the growth solution. The solution was gently mixed for 10 s and left undisturbed at room temperature for at least 6 h before use.

Characterization and Measurement of Photothermal Performance. X-ray diffraction (XRD) measurement was performed on a Bruker D4 X-ray diffractometer using Cu Kα radiation ($\lambda = 0.15418$ nm). Sizes, morphologies, and microstructures of the Cu_9S_5 NCs were determined by a high-resolution transmission electron microscope (HRTEM; JEM-2010F) and a field emission scanning electron microscope (SEM; S-4800). Fourier transform infrared (FTIR) spectra were recorded using the KBr pressed pellets on an IRPRESTIGE-21 spectrometer (Shimadzu). UV−visible absorption spectra were measured on a Shimadzu UV-2550 ultraviolet−visible−near-infrared spectrophotometer using quartz cuvettes with an optical path of 1 cm. Content of copper iron released (from Cu_9S_5 NCs) in the solution was determined by a Leeman Laboratories Prodigy high-dispersion inductively coupled plasma atomic emission spectroscopy (ICP-AES).

For measuring the photothermal conversion performances of these hydrophilic Cu_9S_5 NCs and the comparable Au nanorods, 980 nm NIR laser was delivered through a quartz cuvette containing aqueous dispersion (0.3 mL) of hydrophilic Cu_9S_5 NCs with different concentrations (0−40 ppm), and the light source was an external adjustable power (0−0.3 W) 980 nm semiconductor laser device with a 5 mm diameter laser module (Xi'an Tours Radium Hirsh Laser Technology Co., Ltd. China). The output power was independently calibrated using a handy optical power meter (Newport model 1918-C, CA, USA) and was found to be ~0.29 W for a spot size of ~0.58 cm^2 (*i.e.*, ~0.51 W/cm^2). A thermocouple with an accuracy of ±0.1 °C was inserted into the aqueous dispersion of the Cu_9S_5 NCs perpendicular to the path of the laser. The temperature was recorded one time per 10 s.

Cytotoxicity Assay and PTA of Cancer Cells *in Vivo*. *Cytotoxicity Assay.* The *in vitro* cytotoxicity was measured using the methyl thiazolyl tetrazolium (MTT) assay in human cervical carcinoma cell line HeLa.[3] Cells growing in a log phase were seeded into a 96-well cell culture plate at 5×10^4/well in DMEM (Dulbecco's modified Eagle's medium, which contains 10% fetal bovin serum, 4 mM glutamine, 100 U/mL penicillin, 100 mg/mL streptomycin, and 1% HEPES (hydroxyethyl piperazine ethanesulfonic acid)) at 37 °C and in the presence of 5% CO_2 for 24 h, and then the cells were incubated with the Cu_9S_5 NCs with different concentrations (*i.e.*, 0, 1.6, 3.2, 6.3, 12.5, 25, 50, and 100 ppm, diluted in DMEM) for 24 h at 37 °C in the presence of 5% CO_2. Subsequently, 10 μL of MTT (5 mg/mL) was added to each well of the 96-well assay plate and incubated for more 4 h at 37 °C in the presence of 5% CO_2. After the addition of 10% sodium dodecyl sulfate (SDS, 100 mL/well), the assay plate was allowed to stand at room temperature for 12 h. Multiskan MK3 monochromator-based multifunction microplate reader was used to measure the absorbance of each well with background subtraction at 492 nm. The cytotoxicity of $CuCl_2$ was determined using the same method described for the Cu_9S_5 NCs. All of the tests were independently performed three times.

PTA of Cancer Cells in Vivo. The PTA of cancer cells *in vivo* was carried out by a modified method, as described elsewhere.[45] Severe combined immunodeficiency mice (SCID) were inoculated subcutaneously with 2×10^6 PC-3 cells in the right side of the rear leg 21 days before the experiment. When tumors had grown to 5−10 mm in diameter, the SCID mice were randomly allocated into two groups (control and treatment groups). The SCID mice in the treatment group were injected with 100 μL of Cu_9S_5 NCs' aqueous dispersion (40 ppm) at the central region of the tumor with a depth of ~4 mm, while the SCID mice in the control group were injected with pure water. After 1 h, the tumors inside the SCID mice from both control and treatment groups were irradiated with 980 nm laser at 0.51 W/cm^2 for 10 min. The SCID mice were killed after the laser treatment, and tumors were removed, embedded in paraffin, and cryosectioned into 4 μm slices. The slides were stained with hematoxylin/eosin. The slices were examined under a Zeiss Axiovert 40 CFL inverted fluorescence microscope, and images were captured with a Zeiss AxioCam MRc5 digital camera.

Acknowledgment. This work was financially supported by the National Natural Science Foundation of China (Grant Nos. 21171035, 50872020, 50902021, 20971086, 50925312, and 81071747), the Program for New Century Excellent Talents of the University in China (Grant No. NCET-08-0761), the Science and Technology Commission of Shanghai-based "Innovation Action Plan" Project (Grant No. 10JC1400100), the "Dawn" Program of Shanghai Education Commission, China (Grant No. 08SG32), Shanghai Rising-Star Program (Grant No. 11QA1400100), Shanghai "Chen Guang" project (Grant No. 09CG27), the Fundamental Research Funds for the Central Universities, the National Key Program (973) for Basic Research of China (NO2011CB510106), Shanghai Leading Academic Discipline Project (Grant No. B603) and the Program of Introducing Talents of Discipline to Universities (No. 111-2-04).

Supporting Information Available: The detailed calculation procedures of the molar extinction coefficient and photothermal conversion efficiency, TEM image of the as-prepared Cu_9S_5 NCs, histogram graph showing their volume distribution, UV−vis−NIR absorbance spectra of the Cu_9S_5 NCs dispersed in water at various solution concentrations, the photography of the severe combined immunodeficiency mice bearing s.c. xenografts of PC-3 human prostate cancer cells, experimental setup and heat treatment on the cancerous tissue, H&E stained histological images of the control and treatment group taken at different magnifications, and field emission scanning electron

microscope (SEM) images and energy-dispersive X-ray (EDS) spectra of the tumor slides. This material is available free of charge *via* the Internet at http://pubs.acs.org.

REFERENCES AND NOTES

1. Vogel, A.; Venugopalan, V. Mechanisms of Pulsed Laser Ablation of Biological Tissues. *Chem. Rev.* **2003**, *103*, 577–644.
2. Nolsoe, C. P.; Torppedersen, S.; Burcharth, F.; Horn, T.; Pedersen, S.; Christensen, N. E. H.; Olldag, E. S.; Andersen, P. H.; Karstrup, S.; Lorentzen, T.; *et al.* Interstitial Hyperthermia of Colorectal Liver Metastases with a US-Guided Nd-YAG Laser with a Diffuser Tip: A Pilot Clinical-Study. *Radiology* **1993**, *187*, 333–337.
3. Yang, J.; Choi, J.; Bang, D.; Kim, E.; Lim, E. K.; Park, H.; Suh, J. S.; Lee, K.; Yoo, K. H.; Kim, E. K.; *et al.* Convertible Organic Nanoparticles for Near-Infrared Photothermal Ablation of Cancer Cells. *Angew. Chem., Int. Ed.* **2011**, *50*, 441–444.
4. Whitney, J. R.; Sarkar, S.; Zhang, J. F.; Thao, D.; Young, T.; Manson, M. K.; Campbell, T. A.; Puretzky, A. A.; Rouleau, C. M.; More, K. L.; *et al.* Single Walled Carbon Nanohorns as Photothermal Cancer Agents. *Laser. Surg. Med.* **2011**, *43*, 43–51.
5. Van De Broek, B.; Devoogdt, N.; D'hollander, A.; Gijs, H. L.; Jans, K.; Lagae, L.; Muyldermans, S.; Maes, G.; Borghs, G. Specific Cell Targeting with Nanobody Conjugated Branched Gold Nanoparticles for Photothermal Therapy. *ACS Nano* **2011**, *5*, 4319–4328.
6. Tian, Q.; Tang, M.; Sun, Y.; Zou, R.; Chen, Z.; Zhu, M.; Yang, S.; Wang, J.; Wang, J.; Hu, J. Hydrophilic Flower-like CuS Superstructures as an Efficient 980 nm Laser-Driven Photothermal Agent for Ablation of Cancer Cells. *Adv. Mater.* **2011**, *23*, 3542–3547.
7. Chen, Z. G.; Zhang, L. S.; Sun, Y. G.; Hu, J. Q.; Wang, D. Y. 980-nm Laser-Driven Photovoltaic Cells Based on Rare-Earth Up-Converting Phosphors for Biomedical Applications. *Adv. Funct. Mater.* **2009**, *19*, 3815–3820.
8. Chen, W. R.; Adams, R. L.; Carubelli, R.; Nordquist, R. E. Laser-Photosensitizer Assisted Immunotherapy: A Novel Modality for Cancer Treatment. *Cancer Lett.* **1997**, *115*, 25–30.
9. Chen, W. R.; Adams, R. L.; Higgins, A. K.; Bartels, K. E.; Nordquist, R. E. Photothermal Effects on Murine Mammary Tumors Using Indocyanine Green and an 808-nm Diode Laser: An *In Vivo* Efficacy Study. *Cancer Lett.* **1996**, *98*, 169–173.
10. Huang, N. N.; Wang, H. Q.; Zhao, J. H.; Lui, H.; Korbelik, M.; Zeng, H. S. Single-Wall Carbon Nanotubes Assisted Photothermal Cancer Therapy: Animal Study with a Murine Model of Squamous Cell Carcinoma. *Laser. Surg. Med.* **2010**, *42*, 638–648.
11. Thakare, V. S.; Das, M.; Jain, A. K.; Patil, S.; Jain, S. Carbon Nanotubes in Cancer Theragnosis. *Nanomedicine* **2010**, *5*, 1277–1301.
12. Liu, X. W.; Tao, H. Q.; Yang, K.; Zhang, S. A.; Lee, S. T.; Liu, Z. A. Optimization of Surface Chemistry on Single-Walled Carbon Nanotubes for *In Vivo* Photothermal Ablation of Tumors. *Biomaterials* **2011**, *32*, 144–151.
13. Robinson, J. T.; Welsher, K.; Tabakman, S. M.; Sherlock, S. P.; Wang, H. L.; Luong, R.; Dai, H. J. High Performance *In Vivo* Near-IR (>1 μm) Imaging and Photothermal Cancer Therapy with Carbon Nanotubes. *Nano Res.* **2010**, *3*, 779–793.
14. Fisher, J. W.; Sarkar, S.; Buchanan, C. F.; Szot, C. S.; Whitney, J.; Hatcher, H. C.; Torti, S. V.; Rylander, C. G.; Rylander, M. N. Photothermal Response of Human and Murine Cancer Cells to Multiwalled Carbon Nanotubes after Laser Irradiation. *Cancer Res.* **2010**, *70*, 9855–9864.
15. Zhou, F. F.; Xing, D.; Ou, Z. M.; Wu, B. Y.; Resasco, D. E.; Chen, W. R. Cancer Photothermal Therapy in the Near-Infrared Region By Using Single-Walled Carbon Nanotubes. *J. Biomed. Opt.* **2009**, *14*, 021009.
16. Moon, H. K.; Lee, S. H.; Choi, H. C. *In Vivo* Near-Infrared Mediated Tumor Destruction by Photothermal Effect of Carbon Nanotubes. *ACS Nano* **2009**, *3*, 3707–3713.
17. Ghosh, S.; Dutta, S.; Gomes, E.; Carroll, D.; D'agostino, R.; Olson, J.; Guthold, M.; Gmeiner, W. H. Increased Heating Efficiency and Selective Thermal Ablation of Malignant Tissue with DNA-Encased Multiwalled Carbon Nanotubes. *ACS Nano* **2009**, *3*, 2667–2673.
18. Yang, K.; Zhang, S. A.; Zhang, G. X.; Sun, X. M.; Lee, S. T.; Liu, Z. A. Graphene in Mice: Ultrahigh *In Vivo* Tumor Uptake and Efficient Photothermal Therapy. *Nano Lett.* **2010**, *10*, 3318–3323.
19. Robinson, J. T.; Tabakman, S. M.; Liang, Y. Y.; Wang, H. L.; Casalongue, H. S.; Vinh, D.; Dai, H. J. Ultrasmall Reduced Graphene Oxide with High Near-Infrared Absorbance for Photothermal Therapy. *J. Am. Chem. Soc.* **2011**, *133*, 6825–6831.
20. Lambert, T. N.; Andrews, N. L.; Gerung, H.; Boyle, T. J.; Oliver, J. M.; Wilson, B. S.; Han, S. M. Water-Soluble Germanium(0) Nanocrystals: Cell Recognition and Near-Infrared Photothermal Conversion Properties. *Small* **2007**, *3*, 691–699.
21. Huang, X. Q.; Tang, S. H.; Mu, X. L.; Dai, Y.; Chen, G. X.; Zhou, Z. Y.; Ruan, F. X.; Yang, Z. L.; Zheng, N. F. Freestanding Palladium Nanosheets with Plasmonic and Catalytic Properties. *Nat. Nanotechnol.* **2011**, *6*, 28–32.
22. Tang, S. H.; Huang, X. Q.; Zheng, N. F. Silica Coating Improves the Efficacy of Pd Nanosheets for Photothermal Therapy of Cancer Cells Using Near Infrared Laser. *Chem. Commun.* **2011**, *47*, 3948–3950.
23. Huang, X.; Tang, S.; Liu, B.; Ren, B.; Zheng, N. Enhancing the Photothermal Stability of Plasmonic Metal Nanoplates by a Core−Shell Architecture. *Adv. Mater.* **2011**, *23*, 3420–3425.
24. Wang, S. T.; Chen, K. J.; Wu, T. H.; Wang, H.; Lin, W. Y.; Ohashi, M.; Chiou, P. Y.; Tseng, H. R. Photothermal Effects of Supramolecularly Assembled Gold Nanoparticles for the Targeted Treatment of Cancer Cells. *Angew. Chem., Int. Ed.* **2010**, *49*, 3777–3781.
25. Kim, D.; Jeong, Y. Y.; Jon, S. A Drug-Loaded Aptamer-Gold Nanoparticle Bioconjugate for Combined CT Imaging and Therapy of Prostate Cancer. *ACS Nano* **2010**, *4*, 3689–3696.
26. Park, H.; Yang, J.; Lee, J.; Haam, S.; Choi, I. H.; Yoo, K. H. Multifunctional Nanoparticles for Combined Doxorubicin and Photothermal Treatments. *ACS Nano* **2009**, *3*, 2919–2926.
27. Lee, S. M.; Park, H.; Yoo, K. H. Synergistic Cancer Therapeutic Effects of Locally Delivered Drug and Heat Using Multifunctional Nanoparticles. *Adv. Mater.* **2010**, *22*, 4049–4053.
28. Agarwal, A.; Mackey, M. A.; El-Sayed, M. A.; Bellamkonda, R. V. Remote Triggered Release of Doxorubicin in Tumors by Synergistic Application of Thermosensitive Liposomes and Gold Nanorods. *ACS Nano* **2011**, *5*, 4919–4926.
29. Dickerson, E. B.; Dreaden, E. C.; Huang, X. H.; El-Sayed, I. H.; Chu, H. H.; Pushpanketh, S.; Mcdonald, J. F.; El-Sayed, M. A. Gold Nanorod Assisted Near-Infrared Plasmonic Photothermal Therapy (PPTT) of Squamous Cell Carcinoma in Mice. *Cancer Lett.* **2008**, *269*, 57–66.
30. Huang, H. C.; Rege, K.; Heys, J. J. Spatiotemporal Temperature Distribution and Cancer Cell Death in Response to Extracellular Hyperthermia Induced by Gold Nanorods. *ACS Nano* **2010**, *4*, 2892–2900.
31. Huang, X. H.; El-Sayed, I. H.; Qian, W.; El-Sayed, M. A. Cancer Cell Imaging and Photothermal Therapy in the Near-Infrared Region by Using Gold Nanorods. *J. Am. Chem. Soc.* **2006**, *128*, 2115–2120.
32. Yang, J.; Lee, J.; Kang, J.; Oh, S. J.; Ko, H. J.; Son, J. H.; Lee, K.; Suh, J. S.; Huh, Y. M.; Haam, S. Smart Drug-Loaded Polymer Gold Nanoshells for Systemic and Localized Therapy of Human Epithelial Cancer. *Adv. Mater.* **2009**, *21*, 4339–4342.
33. Ochsenkuhn, M. A.; Jess, P. R. T.; Stoquert, H.; Dholakia, K.; Campbell, C. J. Nanoshells for Surface-Enhanced Raman Spectroscopy in Eukaryotic Cells: Cellular Response and Sensor Development. *ACS Nano* **2009**, *3*, 3613–3621.
34. Bardhan, R.; Chen, W. X.; Perez-Torres, C.; Bartels, M.; Huschka, R. M.; Zhao, L. L.; Morosan, E.; Pautler, R. G.; Joshi, A.; Halas, N. J. Nanoshells with Targeted Simultaneous

Enhancement of Magnetic and Optical Imaging and Photothermal Therapeutic Response. *Adv. Funct. Mater.* **2009**, *19*, 3901–3909.
35. Newhouse, R. J.; Wang, H. N.; Hensel, J. K.; Wheeler, D. A.; Zou, S. L.; Zhang, J. Z. Coherent Vibrational Oscillations of Hollow Gold Nanospheres. *J. Phys. Chem. Lett.* **2011**, *2*, 228–235.
36. Lu, W.; Xiong, C. Y.; Zhang, G. D.; Huang, Q.; Zhang, R.; Zhang, J. Z.; Li, C. Targeted Photothermal Ablation of Murine Melanomas with Melanocyte-Stimulating Hormone Analog-Conjugated Hollow Gold Nanospheres. *Clin. Cancer Res.* **2009**, *15*, 876–886.
37. You, J.; Shao, R. P.; Wei, X.; Gupta, S.; Li, C. Near-Infrared Light Triggers Release of Paclitaxel from Biodegradable Microspheres: Photothermal Effect and Enhanced Antitumor Activity. *Small* **2010**, *6*, 1022–1031.
38. You, J.; Zhang, G. D.; Li, C. Exceptionally High Payload of Doxorubicin in Hollow Gold Nanospheres for Near-Infrared Light-Triggered Drug Release. *ACS Nano* **2010**, *4*, 1033–1041.
39. Zhang, J. Z. Biomedical Applications of Shape-Controlled Plasmonic Nanostructures: A Case Study of Hollow Gold Nanospheres for Photothermal Ablation Therapy of Cancer. *J. Phys. Chem. Lett.* **2010**, *1*, 686–695.
40. Chen, J. Y.; Yang, M. X.; Zhang, Q. A.; Cho, E. C.; Cobley, C. M.; Kim, C.; Glaus, C.; Wang, L. H. V.; Welch, M. J.; Xia, Y. N. Gold Nanocages: A Novel Class of Multifunctional Nanomaterials for Theranostic Applications. *Adv. Funct. Mater.* **2010**, *20*, 3684–3694.
41. Chen, J. Y.; Glaus, C.; Laforest, R.; Zhang, Q.; Yang, M. X.; Gidding, M.; Welch, M. J.; Xia, Y. N. Gold Nanocages as Photothermal Transducers for Cancer Treatment. *Small* **2010**, *6*, 811–817.
42. Ye, E. Y.; Win, K. Y.; Tan, H. R.; Lin, M.; Teng, C. P.; Mlayah, A.; Han, M. Y. Plasmonic Gold Nanocrosses with Multidirectional Excitation and Strong Photothermal Effect. *J. Am. Chem. Soc.* **2011**, *133*, 8506–8509.
43. Hessel, C. M.; Pattani, V. P.; Rasch, M.; Panthani, M. G.; Koo, B.; Tunnell, J. W.; Korgel, B. A. Copper Selenide Nanocrystals for Photothermal Therapy. *Nano Lett.* **2011**, *11*, 2560–2566.
44. Li, Y. B.; Lu, W.; Huang, Q. A.; Huang, M. A.; Li, C.; Chen, W. Copper Sulfide Nanoparticles for Photothermal Ablation of Tumor Cells. *Nanomedicine* **2010**, *5*, 1161–1171.
45. Zhou, M.; Zhang, R.; Huang, M. A.; Lu, W.; Song, S. L.; Melancon, M. P.; Tian, M.; Liang, D.; Li, C. A Chelator-Free Multifunctional [^{64}Cu]CuS Nanoparticle Platform for Simultaneous Micro-PET/CT Imaging and Photothermal Ablation Therapy. *J. Am. Chem. Soc.* **2010**, *132*, 15351–15358.
46. Nakaya, M.; Kanehara, M.; Teranishi, T. One-Pot Synthesis of Large FePt Nanoparticles from Metal Salts and Their Thermal Stability. *Langmuir* **2006**, *22*, 3485–3487.
47. Bu, W. B.; Chen, Z. X.; Chen, F.; Shi, J. L. Oleic Acid/Oleylamine Cooperative-Controlled Crystallization Mechanism for Monodisperse Tetragonal Bipyramid NaLa$(MoO_4)_2$ Nanocrystals. *J. Phys. Chem. C* **2009**, *113*, 12176–12185.
48. Lu, X. M.; Tuan, H. Y.; Chen, J. Y.; Li, Z. Y.; Korgel, B. A.; Xia, Y. N. Mechanistic Studies on the Galvanic Replacement Reaction between Multiply Twinned Particles of Ag and $HAuCl_4$ in an Organic Medium. *J. Am. Chem. Soc.* **2007**, *129*, 1733–1742.
49. Wang, L. Y.; Li, Y. D. $Na(Y_{1.5}Na_{0.5})F_6$ Single-Crystal Nanorods as Multicolor Luminescent Materials. *Nano Lett.* **2006**, *6*, 1645–1649.
50. Zhao, Y.; Pan, H.; Lou, Y.; Qiu, X.; Zhu, J.; Burda, C. Plasmonic $Cu_{2-x}S$ Nanocrystals: Optical and Structural Properties of Copper-Deficient Copper(I) Sulfides. *J. Am. Chem. Soc.* **2009**, *131*, 4253–4261.
51. Luther, J. M.; Jain, P. K.; Ewers, T.; Alivisatos, A. P. Localized Surface Plasmon Resonances Arising from Free Carriers in Doped Quantum Dots. *Nat. Mater.* **2011**, *10*, 361–366.
52. Kam, N. W. S.; O'connell, M.; Wisdom, J. A.; Dai, H. Carbon Nanotubes as Multifunctional Biological Transporters and Near-Infrared Agents for Selective Cancer Cell Destruction. *Proc. Natl. Acad. Sci. U.S.A.* **2005**, *102*, 11600–11605.
53. Nikoobakht, B.; Wang, J.; El-Sayed, M. A. Surface-Enhanced Raman Scattering of Molecules Adsorbed on Gold Nanorods: Off-Surface Plasmon Resonance Condition. *Chem. Phys. Lett.* **2002**, *366*, 17–23.
54. Hirsch, L. R.; Stafford, R. J.; Bankson, J. A.; Sershen, S. R.; Rivera, B.; Price, R. E.; Hazle, J. D.; Halas, N. J.; West, J. L. Nanoshell-Mediated Near-Infrared Thermal Therapy of Tumors under Magnetic Resonance Guidance. *Proc. Natl. Acad. Sci. U.S.A.* **2003**, *100*, 13549–13554.
55. Roper, D. K.; Ahn, W.; Hoepfner, M. Microscale Heat Transfer Transduced by Surface Plasmon Resonant Gold Nanoparticles. *J. Phys. Chem. C* **2007**, *111*, 3636–3641.
56. Link, S.; El-Sayed, M. A. Shape and Size Dependence of Radiative, Non-radiative and Photothermal Properties of Gold Nanocrystals. *Int. Rev. Phys. Chem.* **2000**, *19*, 409–453.
57. Chen, H. J.; Shao, L.; Ming, T. A.; Sun, Z. H.; Zhao, C. M.; Yang, B. C.; Wang, J. F. Understanding the Photothermal Conversion Efficiency of Gold Nanocrystals. *Small* **2010**, *6*, 2272–2280.
58. Cole, J. R.; Mirin, N. A.; Knight, M. W.; Goodrich, G. P.; Halas, N. J. Photothermal Efficiencies of Nanoshells and Nanorods for Clinical Therapeutic Applications. *J. Phys. Chem. C* **2009**, *113*, 12090–12094.
59. Yang, H.; Zhang, C. X.; Shi, X. Y.; Hu, H.; Du, X. X.; Fang, Y.; Ma, Y. B.; Wu, H. X.; Yang, S. P. Water-Soluble Superparamagnetic Manganese Ferrite Nanoparticles for Magnetic Resonance Imaging. *Biomaterials* **2010**, *31*, 3667–3673.
60. Chen, Z.; Tian, Q.; Song, Y.; Yang, J.; Hu, J. One-Pot Synthesis of $Zn_xCd_{1-x}S$ Nanocrystals with Tunable Optical Properties from Molecular Precursors. *J. Alloys Compd.* **2010**, *506*, 804–810.